$Q^{(n)}$-Species Distribution in $K_2O \cdot 2\ SiO_2$ Glass by ^{29}Si Magic Angle Flipping NMR

THESIS

Presented in Partial Fulfillment of the Requirements for

Research with Distinction in Chemistry

in the undergraduate colleges of The Ohio State University

By

Derrick C. Kaseman,

* * * * *

The Ohio State University

2011

Thesis Committee:

Professor Sherwin Singer

Professor Philip J. Grandinetti, Adviser

Approved by

Adviser

Department of Chemistry

ABSTRACT

Two-dimensional magic angle flipping (MAF) was employed to measure the $Q^{(n)}$ distribution in a ^{29}Si enriched potassium disilicate glass ($K_2O \cdot 2\ SiO_2$). Relative concentrations of $[Q^{(4)}] = 7.23\% \pm 0.339\%$, $[Q^{(3)}] = 82.97\% \pm 0.118\%$, $[Q^{(2)}] = 9.80\% \pm 0.660\%$ were obtained. Using the thermodynamic model for $Q^{(n)}$-species disproportionation these relative concentrations yield an equilibrium constant $k_3 = 0.01029 \pm 0.00084$, indicating, as expected, that the $Q^{(n)}$-species distribution is close to binary in the potassium disilicate glass. A Gaussian distribution of isotropic chemical shifts was observed for each $Q^{(n)}$-species with mean values of -82.74 ± 0.03 ppm, -91.32 ± 0.00 ppm, and -101.67 ± 0.02, and standard deviations of 3.27 ± 0.03 ppm, 4.194 ± 0.003 ppm, and 5.09 ± 0.03 for $Q^{(2)}$, $Q^{(3)}$, and $Q^{(4)}$, respectively. Additionally, nuclear shielding anisotropy values of $\zeta = -85.0 \pm 1.3$ ppm, $\eta = 0.48 \pm 0.02$ for $Q^{(2)}$, and $\zeta = -74.9 \pm 0.2$ ppm, $\eta = 0.030 \pm 0.006$ for $Q^{(3)}$ were observed in the potassium disilicate glass.

This is dedicated to my sister, Justine Kaseman.

ACKNOWLEDGMENTS

I would like to take this opportunity to thank all of those who have supported me on my academic journey. I would especially like to thank my parents, Jeffrey and Kim Kaseman, who have kept me continuously motivated . Their constant encouragement has been instrumental in this process. I would also like to thank the Brothers of the Omicron Deuteron Chapter of Phi Gamma Delta for shaping my college experience. In addition, I thank Dr. Michael C. Davis for his advice. Finally, I would like to thank Dr. Philip Grandinetti for his support and guidance over the years. Working in his lab has been one of the greatest experiences I've ever had. His constant guidance and patience has helped me learn more than any class could teach.

TABLE OF CONTENTS

Page

LIST OF FIGURES

Figure **Page**

LIST OF TABLES

Table **Page**

CHAPTER 1

Introduction

1.1 Glass

1.1.1 History of Glass

Glassy materials have and continue to be an integral part of human civilization [1–16]. Man first used obsidian, a naturally occurring volcanic glass, to make weapons and tools [9,10,14]. The first man-made glass was created in the Middle East around five thousand years ago [1, 13]. Reserved for royalty, early glass was fragile, opaque, and used only as drinking vessels [9, 13]. Early glass was difficult to make until the Roman Empire developed glass blowing which allowed for the mass production of glass. Glass blowing led to speedy creation of glasses with varying compositions which made glass available to all social classes [4, 9, 13]. As the Roman Empire declined, religious idealism promoted the use of glass in the Middle East [9]. For example, the Koran forbade material wealth, so many people turned towards the use of glass to create the illusion of luxury. The center of glass creation then shifted to Venice, Italy during the Renaissance. During this time, glass was primarily used as an art medium to create glass beads, glass mirrors, and crystal glass, most of which was reserved for royalty [9, 13]. The Roman Catholic church used glass to make, unbeknown to them, nanoparticle containing stained glass windows [11,14]. During this time period

in England, lead glasses were created for bottling and shipping needs [9, 13, 17]. The growing glass industry then shifted to America. As America's first industry, glass-makers focused on making bottles and windows. The American glass industry sped up the glass making process, for the first time since the Roman Empire, with the creation of a machine press that made glass. The American glass industry also contributed an automatic bottle blowing machine that has become invaluable across many different industries today [9]. For centuries, glass technology has fueled scientific investigations; from the glass in Galileo's telescope [13, 14], to corrective lenses [7], to the research done by Descartes and Snell [13], to the volumetric glassware used in laboratories world-wide.

1.1.2 Defining Glass

Although glass has been around for over five millennia [1,9], a precise definition of a glass has been a challenge [13]. According to Zarzycki [14], a glass can be narrowly defined as a solid obtained by supercooling a liquid without crystallization, or more broadly defined as simply a non-crystalline solid. The first definition is restrictive because some glasses can also be formed by using precipitation reactions [18, 19], polymerization reactions, and electrolytic deposition [20, 21]. Additionally, glasses are not limited to formation from liquids; there are several techniques to create glass from solids and gases [22–30]. The second definition broadly encompasses glasses, ceramics, gels, and some nano-structures. Here, we will side step these semantics issues, and focus on the determination of atomic-level structure in non-crystalline solids, which include glasses [14].

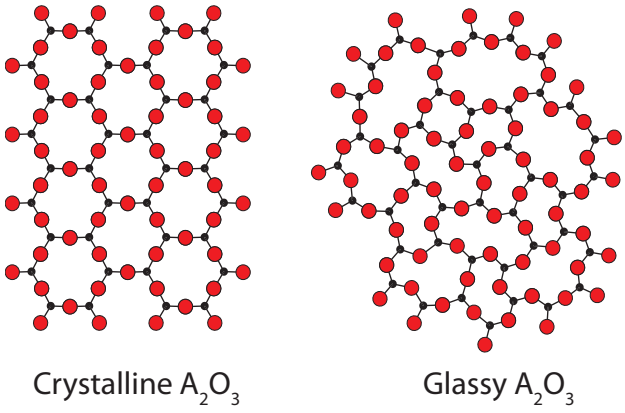

Figure 1.1: Two dimensional schematic representation of the Zacharisen model [33] (right), that describes a glass having local (first-coordination sphere) structure order but lacking long-range structural periodicity, in contrast to a crystalline solid (left)

1.1.3 Structural and Thermodynamic Models

Due to the amorphous nature of glass, atomic-level structural details have been challenging to elucidate [15,31,32]. Therefore, the structure of glass is first characterized by its short-range bonding order, which consists of a central atom coordinated to ligands (first-coordination sphere). The Zachariasen model [33], shown in Figure 1.1 explains that silicon dioxide glass is composed of a network of silica polyhedron linked by oxygen at various angles. With the introduction of network modifier cations, solid-surface interactions between the glass and modifying cation decreased the melting temperature of the glass, allowing for glass to be created by early civilizations.

The short range bonding environment in silicate glasses described by Zacharisen [33] has been confirmed experimentally using XRD, neutron diffraction, and infrared (IR) spectroscopy [34–40]. Diffraction experiments, first by Mozzi and Warren [41], and later by Neuefeind and Liss [42], obtained the radial distribution function, $T_x(r)$,

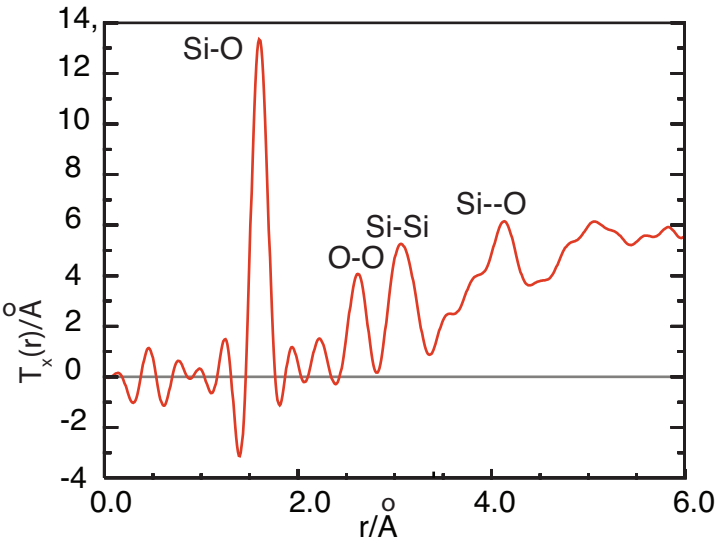

Figure 1.2: Radial distribution function, $T_x(r)$, of a silica [42] where r is the distance from the origin in units of Angstroms.

from the Fourier transform of the acquired x-ray diffraction data. The radial distribution function is a measure of the density of atoms at a distance, r, from the atom of interest [43], as shown in Fig. 1.2. The diffraction results [42] also indicate that a range of interatomic Si-Si distances exist in silica, further indicating a range of bond angles between silicon and oxygen. In addition to silicate glasses, XRD and neutron diffraction has also been used to confirm Zacharisen's structure model in germanium oxide [39], titanium oxide [44], and barium oxide [38] glasses.

The commonplace practice of using network modifying cations to alter the chemical properties of glass led Zachariasen to propose a further structural model [33], illustrated in Figure 1.3, to account for these changes. In this model, network modifying cations (Na^+, K^+, Mg^{2+}, Ca^{2+}, etc.) coordinate to oxygen and depolymerize the silicate network. Experimental studies by Warren and Biscoe [35] used x-ray diffraction

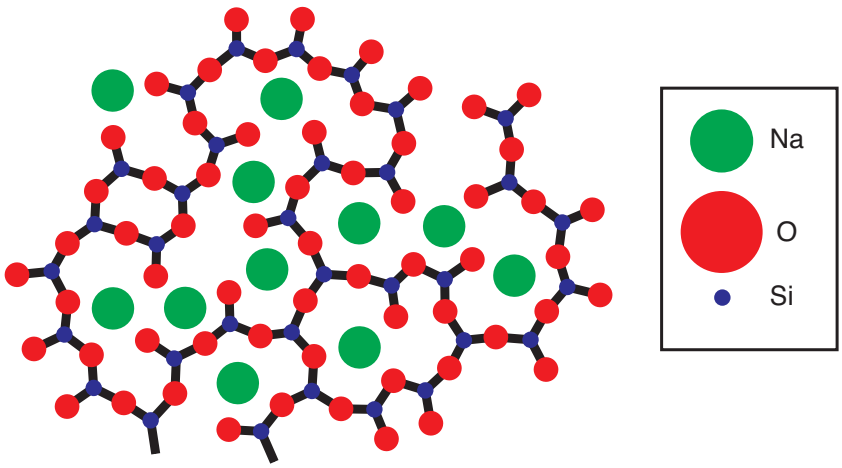

Figure 1.3: Random network model proposed by Warren and Biscoe [35] in which the network modifying cations are randomly spread throughout the glass. R represents either an alkali metal or an alkali earth metal.

(XRD) to examine the structure of network modified silicate glasses. Their results indicate that, in contrast to having an ordered distribution of modifying cations within the glass structure, as proposed by Zachariasen [33], modifying cations are randomly throughout the glass, as illustrated in Figure 1.3. In both models, network modifying cations break Si-O-Si linkages between silicate tetrahedra. Oxygen can be divided into two types, those that are corner sharing between two silicate tetrahedra, called bridging oxygen (BO), and the more negatively charged terminal oxygen on silicate tetrahedra, called non-bridging oxygen (NBO). The network modifying cations are coordinated near the non-bridging oxygen [14].

In 1985, Greaves [45] proposed the modified random network model, where the distribution of network modifying cations in the glass is not expected to be purely random, as proposed by Warren and Biscoe [35]. Instead, the network modifying cations

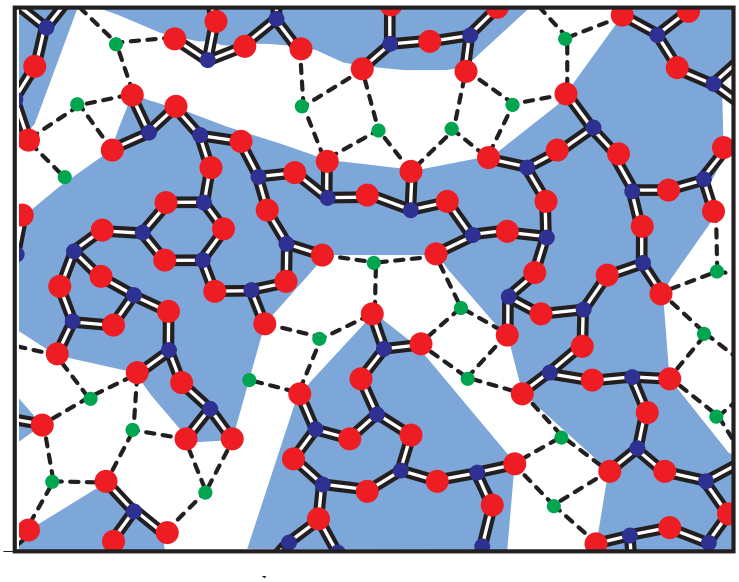

Figure 1.4: The modified random network model, proposed by Greaves [45], where network modifying cations (green/small circles) form channels in the glass. The silicon (blue/medium circles) and oxygen (red/large circles) form a polymerized random network.

cluster together to form ion channels within the silica-oxygen polymer network, as illustrated in Figure 1.4.

One possible way to test these different structure models of how NBO are distributed within the bulk glass is to examine the thermodynamic model for the disproportionation equilibria of $Q^{(n)}$-species, where $Q^{(n)}$ represents a silicate tetrahedron and n is the number of BO per silicon tetrahedron, ranging from $n = 0$ to $n = 4$. This thermodynamic model, proposed by Bray and coworkers [46], is given by the reaction:

$$2Q^{(n)} = Q^{(n+1)} + Q^{(n-1)} \qquad \text{where } n = 3, 2, 1. \tag{1.1}$$

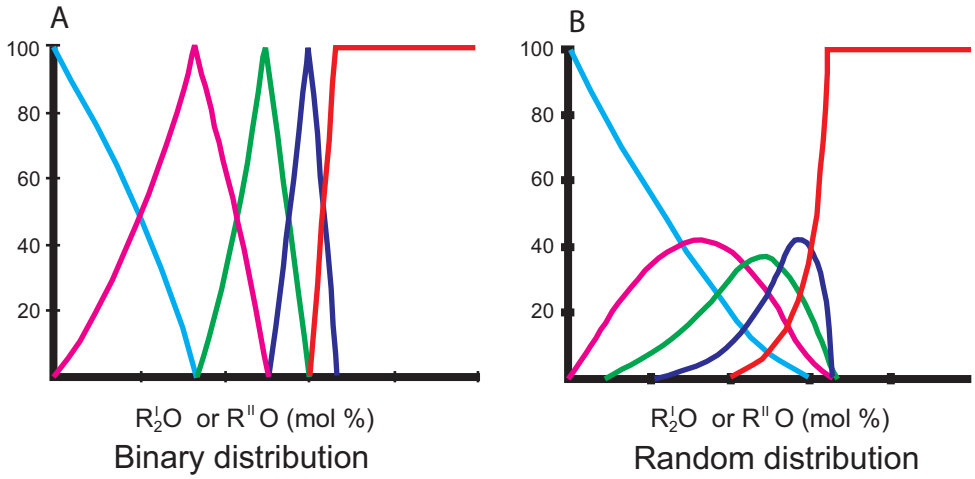

Figure 1.5: (A) Binary and (B) random distribution of $Q^{(n)}$-species in thermodynamic model of $Q^{(n)}$-species disportionation [48].

The $Q^{(n)}$ concentrations are used to calculate a disproportionation constant k_n, given by

$$k_n = \frac{[Q^{(n+1)}][Q^{(n-1)}]}{[Q^{(n)}]^2}. \tag{1.2}$$

If the distribution of $Q^{(n)}$ in the glass is binary, then k_3, k_2, and k_1 will be zero. If the distribution is random, then $k_3 = 0.375$, k_2=0.495 , and k_1=0.311 [46, 47].

Raman spectroscopy has been used to identify different $Q^{(n)}$-species present in glasses [13, 49–51]. Additionally, Raman studies has been successful in describing medium-range bonding order, and studies by Malfait et al. [52] have observed that glasses with high alkali concentrations are composed of 4-6 membered rings of silicon tetrahedra. Their results were similar to studies of other glasses where distinct stretches are observed corresponding to the stretching and bending within the ring structures [49, 53–57]. While XRD, IR, and Raman techniques are useful in studying

the short range bonding order in network modified glasses, neither of these techniques is inherently quantitative preventing accurate quantification of different $Q^{(n)}$-species present within the glass.

Nuclear magnetic resonance (NMR) spectroscopy, however, has proven useful in quantifying different $Q^{(n)}$-species [58–60], since NMR is able to separate nuclei in different bonding environments through a distinct resonance shift that is observed in the NMR spectrum. The relative abundance of each $Q^{(n)}$-species can then be obtained through the total integrated area of the assigned resonance. A binary distribution of $Q^{(n)}$-species, illustrated in Figure 1.5A and experimentally observed by Bray and Dupree et al. [61, 62] in ^{29}Si NMR studies of soda-lime glasses, has only two $Q^{(n)}$-species with the sequential appearance of other $Q^{(n)}$-species as the alkali content increases. Initially, a glass containing no network modifying cation, such as quartz glass, has only $Q^{(4)}$ sites. As network modifying cations are introduced into the glass, the concentration of the $Q^{(4)}$ decreases to zero as the concentration of $Q^{(3)}$ increases to 100%. This trend continues until enough network modifying cation is added that only $Q^{(0)}$ sites remain. For a random distribution, each $Q^{(n)}$-species can exist within the glass at a given concentration of modifying cation, where the probabilities of observing each $Q^{(n)}$-species is determined by the constraints of mass and charge balance.

1.2 Nuclear Magnetic Resonance

1.2.1 Overview

Developed in 1945, NMR is a spectroscopic technique that can be to used identify and quantify nuclei present in a sample as well as discriminate between nuclei in different bonding environments.

Macroscopic Model of Atomic Nuclei

To understand NMR it is helpful to use the analogy of the atomic nucleus as a spinning top with a magnetic dipole moment along the spinning axis. If an external magnetic field, B_0, is applied to the magnetic top (nucleus), it will precess about the external magnetic field, as illustrated in Figure 1.6, with a precession frequency given by

$$\omega = \gamma B_0 \tag{1.3}$$

where γ is the gyromagnetic ratio of the magnetic top, which is the ratio of the magnetic dipole moment to angular momentum of the magnetic top. As we can see from Eq. 1.3, the precessional frequency of the magnetic top is proportional to the strength of the applied magnetic field. If a loop of wire is placed parallel to B_0, the top will pass through the loop inducing an electromotive force (EMF) in the wire, as illustrated in Figure 1.7. We use Faraday's Law,

$$\text{EMF} = -\frac{d\Phi}{dt}, \tag{1.4}$$

to quantify the EMF induced from the precessional frequency. Here $d\Phi$ is the magnetic flux. The EMF induced by the top as it precesses about B_0 is given by

$$EMF = \omega_0 \frac{\mu_0}{2r_{coil}} |\mu| \sin(\psi) \sin(\omega_0 t + \xi_0) \tag{1.5}$$

where ω_0 is the precession frequency, $|\mu|$ is the length of the precessing magnetization vector, ψ is the angle between the z axis and the precessing magnetization vector, and ξ_0 is the initial phase of the vector, as illustrated in Figure 1.8.

If we place a sample containing a ensemble of uncoupled magnetic tops ($\approx 10^{20}$) in a magnetic field, there will initially be a random distribution of angles (ψ, ξ_0) about

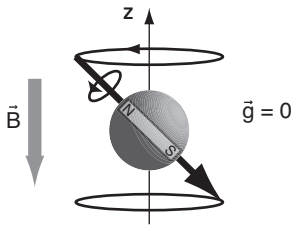

Figure 1.6: A spinning magnetic top in a zero gravity environment precessing about the applied external magnetic field B_0.

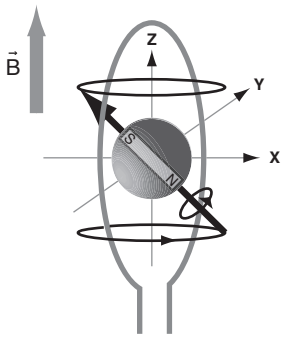

Figure 1.7: A spinning magnetic top precessing about B_0 will induce an EMF in a coil wrapped parallel to B_0.

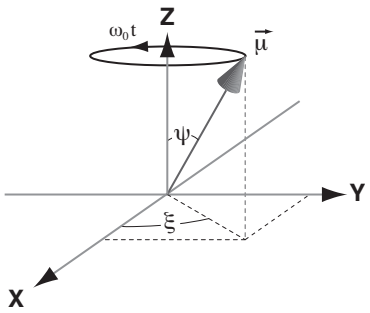

Figure 1.8: Magnetization vector $\vec{\mu}$ as it precesses about B_0.

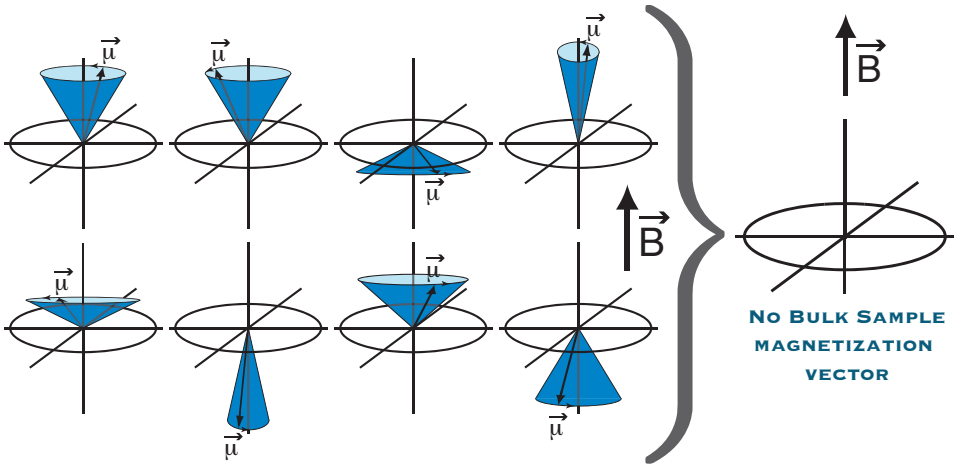

Figure 1.9: A sample will contain an magnetization vectors, $\vec{\mu}$, precessing at different angles all precessing around B_0. Before achieving thermal equilibrium, all of these vectors cancel, leaving no bulk magnetization vector

which the tops precess, as illustrated in Figure 1.9, creating a net magnetization vector of zero, and thus, a net EMF that is also zero. The sample will eventually come to thermal equilibrium at which there will be a Boltzmann distribution of magnetic moments above and below the xy plane. The difference between the magnetic moments above and below the xy plane create a net magnetic moment along the z axis, as illustrated in Figure 1.10.

Magnetic Resonance

Although a net magnetization vector is obtained at thermal equilibrium, the vector can not be detected since it lies parallel to the magnetic field. To overcome this, magnetic resonance is used, illustrated in Figure 1.11, in which a small magnetic field, B_1, is applied along +x axis. The net magnetization becomes slightly tilted away from B_0 toward the $-x$ axis. The spins precess 180° and B_1 is then applied

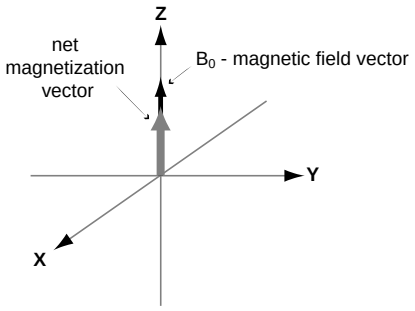

Figure 1.10: After the sample reaches a thermal equilibrium, the distribution of spins in the $+xy$ plane will be greater than the distribution of spins in the -xy plane. This creates a net magnetization along the $+z$ axis

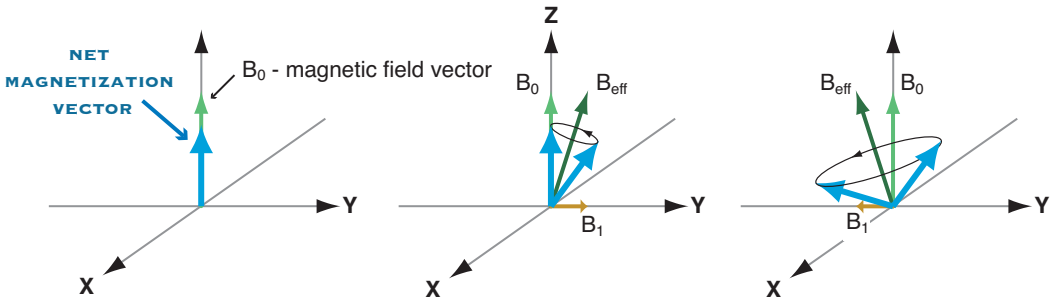

Figure 1.11: A small magnetic field B_1 is applied along the $+y$ axis (black arrow). This causes the net magnetization, originally along $+z$ to tilt slightly toward the $+y$ axis. Once the magnetization precesses 180° B_1 is applied along the $-y$ axis which increases the tilt of the magnetization vector away from B_0

along the $-x$ axis. This causes the tilt from B_0 to become greater. This process is repeated until the bulk magnetization lies along the x-y plane. The magnetization will then precess around B_0, in and out of the plane of the detector coil, creating a measurable EMF.

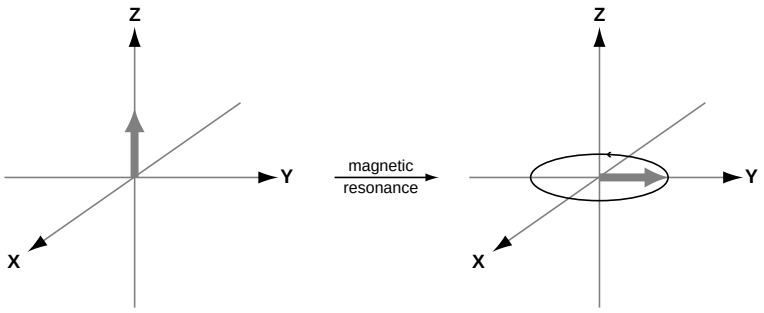

Figure 1.12: During magnetic resonance, alternating small magnetic fields are applied to the bulk magnetization which shifts the bulk magnetization from the $+z$ axis to the xy plane

Nuclear Shielding and Chemical Shift

One of the main advantages of NMR is the separation of nuclei on the basis of nuclear shielding. The magnetic field experienced by a nucleus is directly affected by the electronic environment around the nucleus. The external magnetic field, B_0, induces a current in the electrons which, in turn induces a magnetic field that reduces the net magnetic field at the nucleus. The nucleus will be more shielded if there is a larger density of electrons around the nucleus. Thus, the nuclear shielding can be used to distinguish nuclei in different bonding environments. The shielding of the nucleus modifies the precession frequency in an isotropic system according to

$$\omega = \gamma(1 - \sigma_{\text{iso}})B_0, \tag{1.6}$$

where σ_{iso} is the isotropic nuclear shielding, calculated from the full nuclear shielding tensor according to

$$\sigma_{\text{iso}} = \frac{1}{3}(\sigma_{xx} + \sigma_{yy} + \sigma_{zz}), \tag{1.7}$$

where σ_{xx}, σ_{yy}, and σ_{zz} are the diagonal components of the nuclear shielding tensor. In the NMR experiment the nuclear shielding is not measured directly since we would need a reference spectra with respect to a completely deshielded nucleus, which is not physically possible. Instead, resonances are assigned with respect to a standardized reference compound, such as tetramethylsilane (TMS) for ^{29}Si, referred to as the isotropic chemical shift, δ_{iso}, and given by

$$\delta_{iso} = \frac{(\sigma_{ref} - \sigma_{iso})}{(1 - \sigma_{ref})}, \tag{1.8}$$

where σ_{ref} is the isotropic nuclear shielding of a reference compound.

As illustrated in Figure 1.13, the silicon nucleus in each $Q^{(n)}$-species is less shielded than the silicon nucleus in the TMS reference (δ_{iso}=0), resulting in a negative chemical shift for all $Q^{(n)}$-species. As the silicon nucleus in the $Q^{(n)}$-species becomes more shielded, its isotropic position shifts downfield in the NMR spectrum. This is also illustrated in Figure 1.13 in the case of a ^{29}Si nucleus in different $Q^{(n)}$ environments. Of the five $Q^{(n)}$ environments, the silicon in the $Q^{(4)}$ site has the smallest electron density at the nucleus and the smallest nuclear shielding. The isotropic chemical shift for $Q^{(4)}$, therefore, will have the most negative shift, as observed in experiment -110 ppm. In contrast, the $Q^{(0)}$ site has the largest electron density and the largest nuclear shielding, with an isotropic chemical shift around -60 ppm (downfield shift from $Q^{(4)}$). The isotropic chemical shifts for $Q^{(1)}$, $Q^{(2)}$, and $Q^{(3)}$, which have medium electron densities and nuclear shieldings, range from -70 ppm to -100 ppm.

In liquid samples, the rapid reorientation of molecules averages the nuclear shielding and only a single isotropic contribution to the NMR frequency is observed. In solids, however, the nuclear shielding tensor results in anisotropic nuclear shielding contributions to the NMR frequency. Thus, a broad anisotropic powder pattern in

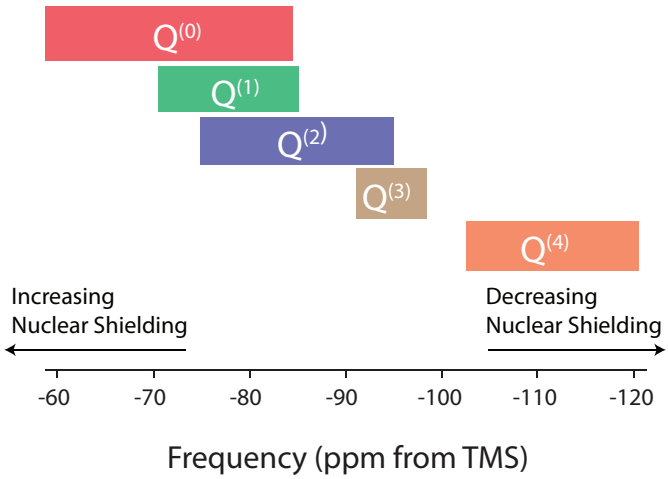

Figure 1.13: Isotropic chemical shift ranges for each $Q^{(n)}$-species [63]

polycrystalline samples is observed, as illustrated in figure 1.14. The principal values of the nuclear shielding tensor can be obtained through direct analysis of the observed NMR lineshape, as also illustrated in Figure 1.14. Following the Haeberlen convention [64], where

$$|\sigma_{zz} - \sigma_{\text{iso}}| > |\sigma_{yy} - \sigma_{\text{iso}}| > |\sigma_{xx} - \sigma_{\text{iso}}|, \tag{1.9}$$

the anisotropy can be described using the magnitude of the nuclear shielding anisotropy, ζ, given by

$$\zeta = \sigma_{zz} - \sigma_{\text{iso}}, \tag{1.10}$$

and the asymmetry parameter, η, given by

$$\eta = \frac{\sigma_{yy} - \sigma_{xx}}{\zeta}. \tag{1.11}$$

While this anisotropic line broadening presents a resolution and sensitivity challenge for the NMR spectroscopist, knowledge of the principal values of the nuclear shielding

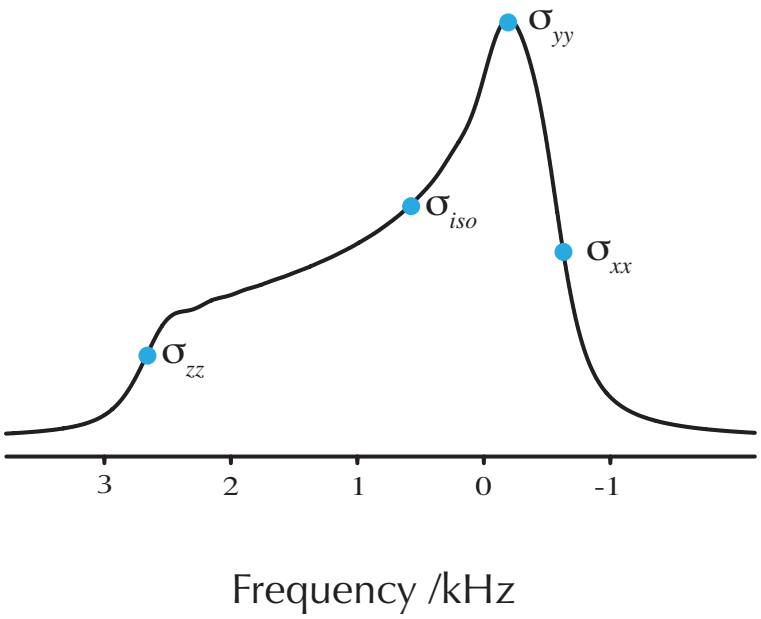

Figure 1.14: Nuclear shielding parameters and their effect on the NMR lineshape in a polycrystalline sample.

tensor can provide additional structural detail about local electronic structure around the nucleus.

Stebbins [59] observed that each $Q^{(n)}$-species in the ^{29}Si NMR spectrum will unique parameters for ζ and η because of the different chemical environments around the ^{29}Si nucleus. As the symmetry of the electron density about the ^{29}Si nucleus decreases, ζ increases. For example, for $Q^{(4)}$ and $Q^{(0)}$, where the ^{29}Si nucleus resides in a symmetric bonding environments, ζ and η will be zero because $\sigma_{zz} = \sigma_{yy} = \sigma_{xx}$. In contrast, ^{29}Si for $Q^{(1)}$, $Q^{(2)}$, and $Q^{(3)}$ sites will be in an asymmetrical bonding environment because there will be different number of bridging and nonbridging oxygen around ^{29}Si and ζ and η will be nonzero. The ability of NMR to probe the local bonding environment allows multiple $Q^{(n)}$-species to be resolved in the NMR spectrum since

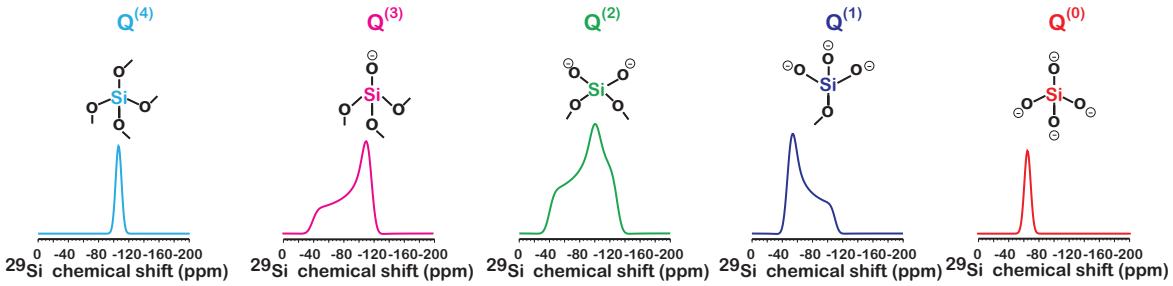

Figure 1.15: Anisotropic lineshapes for each $Q^{(n)}$-species [63]

each for each $Q^{(n)}$ has a characteristic lineshape with a unique isotropic chemical shift will be observed, as illustrated in Figure 1.15. The anisotropic lineshapes of the $Q^{(n)}$-species span over large frequency ranges which create complicated NMR spectra when more that one $Q^{(n)}$-species is present. One way to overcome the broad anisotropic lineshapes and quantify the $Q^{(n)}$-species is to perform magic angle spinning on the sample.

1.2.2 Magic Angle Spinning

Magic angle spinning (MAS) averages the frequency anisotropy in powdered solids by mimicking the natural reorientation that occurs in liquids by rapidly spinning the sample in a packed rotor at a fixed angle during the NMR experiment. Typically, this angle is chosen to be the "magic angle" [65], which is 54.74° with respect to the external magnetic field. Under MAS, second-rank anisotropic interactions are averaged to zero assuming the spinning speed is greater than the width of the underlying anisotropy. If the spinning speed is less than the width of the anisotropy, then a series of spinning sidebands that occur at integer multiples of the spinning speed will be observed in the NMR spectrum, as shown in figure 1.16. Since NMR is

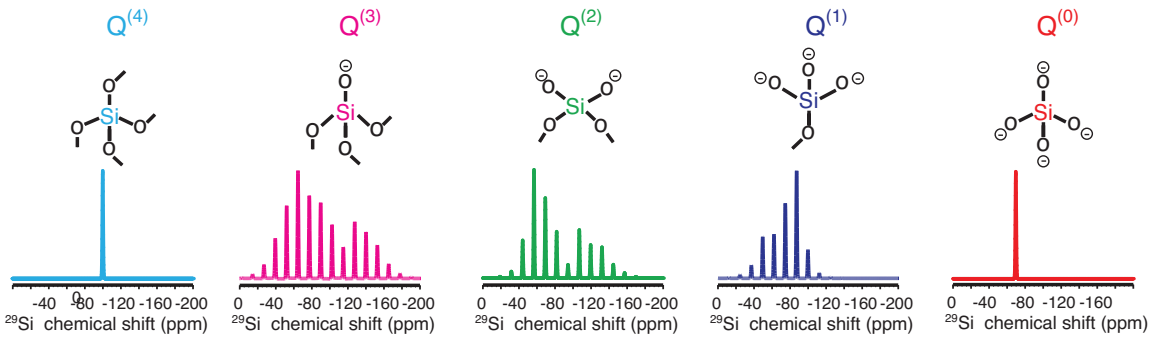

Figure 1.16: Spinning sidebands occur when the spinning speed of the sample is less than the width of the anisotropy. Above are the spinning sideband patterns for each $Q^{(n)}$-species.

a quantitative analytical technique, averaging the anisotropy through MAS increases sensitivity since the total integrated area of the broad powder pattern, observed during static experiments, is collapsed into a narrow resonance. Each $Q^{(n)}$ chemical shift range is well known [66–68]. While high speed MAS of glass averages away the frequency anisotropy, broad overlapping Gaussian lineshapes are still observed due to a distribution of isotropic chemical shifts, which, in turn, arises from a structural distributions around the $Q^{(n)}$ sites [69]. Typically, a MAS lineshape can be deconvoluted with the assumption that each $Q^{(n)}$ site's contributions to the spectrum can be represented as a Gaussian lineshape. While there have been many previous MAS studies [52, 60, 70–72] on the structure of silicate glasses, spectral resolution is often hindered by this broad overlap of Gaussian lineshapes.

1.2.3 Magic Angle Flipping

To overcome the limitations of fitting the spectrum with a series of broad overlapping Gaussian functions when multiple $Q^{(n)}$ are present in the glass, we can employ

2D correlation experiments that combine the benefits of static NMR, where we observe broad pattern patterns that contain structural details about the local bonding environment, and the MAS experiment, where we observe narrow lineshapes that can be separated into distinct frequency regions for each $Q^{(n)}$-species. Two-dimensional experiments correlating an isotropic dimension to an anisotropic dimension include Magic Angle Hopping (MAH) [73], Magic Angle Flipping (MAF) [73], and 2D Phase Adjusted Spinning Sidebands (PASS) [74, 75].

The 2D MAF experiment manipulates the spatial dependence of the anisotropy by reorienting the rotor axis during the experiment between two angles, 90° and 54.74°, with respect to the external magnetic field. At the beginning of the experiment, the magnetization is allowed to evolve for a variable evolution time, t_1, where the rotor is spun at 90° with respect to the external magnetic field. Since the magnitude of the anisotropy scales with the second-rank Legendre polynomial, $P_2(\cos\theta)$, spinning the rotor axis introduces the anisotropy during t_1 since $P_2(\cos\theta)$ = -0.5. Following the evolution period the magnetization is stored as the rotor axis is mechanically flipped back to the magic angle, where $P_2(\cos\theta) = 0$ and the anisotropy is fully averaged, and the signal detected. The resulting 2D signal will be amplitude modulated in t_1 by the relative contribution from the anisotropy. A 2D Fourier transform of the dataset will then give a frequency domain spectrum that correlates a narrow dimension with only anisotropic present and a broad anisotropic dimension that has contributions from both the isotropic and anisotropy frequencies. Based on the unique isotropic chemical shift of the $Q^{(n)}$ sites, we can fit the cross sections of the data by fixing the isotropic chemical shift of each cross section. Using the ζ and η parameters of the chemical shift as constraints on the lineshape, we can integrate the peak area of

each cross section and obtain the relative concentrations of the $Q^{(n)}$-species. There are limitations to this technique including the flipping between angles, which requires specialized hardware, and the signal in the MAS dimension is reduced [73, 76].

The next chapter will focus on using MAF to determine the $Q^{(n)}$-species in a potassium disilicate glass. The relative abundances will provide insight into the structural and thermodynamic models for potassium silicate glasses.

CHAPTER 2

Determination of Anionic Species within a Potassium Disilicate Using MAF

2.1 Introduction

In earlier work Zhang et al. [77, 78] utilized the MAF NMR experiment [79, 80], which produces a two dimensional (2D) spectrum correlating isotropic and anisotropic nuclear shielding contributions to the solid-state spectrum, can be used to give over an order of magnitude improvement in quantifying $Q^{(n)}$-species concentrations when compared to conventional ^{29}Si Magic-Angle Spinning (MAS) lineshape analysis. Additionally, this method does not require the assumption of a Gaussian distribution of isotropic ^{29}Si chemical shifts for the different $Q^{(n)}$-species. Its accuracy and precision were demonstrated in a well-understood sodium silicate glass binary composition [77] yielding a value of $k_3 = 0.0129 \pm 0.0001$. The same approach was applied successfully on a $CaO_2 \cdot SiO_2$ glass [78], which has a completely unresolved ^{29}Si MAS spectrum, to obtain the equilibrium constants $k_1 = 0.105 \pm 0.019$, $k_2 = 0.156 \pm 0.005$, and $k_3 = 0.106 \pm 0.022$ for the disproportionation reactions in $CaO_2 \cdot SiO_2$. These latter results were the first quantitative measure of $Q^{(n)}$ distributions in the alkaline earth silicate glass, and indicated a significantly greater deviation from a binary

model of $Q^{(n)}$-species disproportionation in alkaline earth silicate melts compared to alkali silicate melts.

Since 2D MAF requires a solid-state NMR probe with specialized hardware to reorient the sample rotation axis, it should also be noted that there are a number of alternative solid-state methods for obtaining the same 2D correlation of isotropic and anisotropic nuclear shielding contributions [74,75,81–83], some of which have also been applied to glasses [84–89]. In addition to improved quantification of $Q^{(n)}$-species, 2D double-quantum NMR techniques have also been used to establish connectivities between $Q^{(n)}$-species by exploiting dipolar couplings [90–93] and more recently through J couplings [52,94,95]. These experiments have also provided more accurate mean chemical shifts for $Q^{(n)}$ sites to aid in deconvolution of overlapping Gaussian lineshapes in MAS spectra.

Recently, Florian and coworkers [95] found, through *ab initio* calculations calibrated with experimental measurements in crystalline phases, a close-to-linear relationship between the $^2J_{\text{Si-O-Si}}$ coupling and the Si–O–Si bond angle. Additionally, they measured a 2D J-resolved MAS spectrum, which correlates ^{29}Si isotropic chemical shifts and $^2J_{\text{Si-O-Si}}$ couplings, for a ^{29}Si-enriched $CaO_2 \cdot SiO_2$ glass. Generally, the intensity in a ^{29}Si MAS lineshape of a fully ^{29}Si-enriched silicate glass at a given isotropic chemical shift can contain contributions from any of the $Q^{(n)}$ sites, and a ^{29}Si nucleus in a given $Q^{(n)}$ will experience n different $^2J_{\text{Si-O-Si}}$ couplings. Thus, critical in the analysis of the 2D J-resolved MAS spectrum of $CaO_2 \cdot SiO_2$ glass were the ^{29}Si chemical shift distributions for the five $Q^{(n)}$ populations in $CaO_2 \cdot SiO_2$ glass derived from the ^{29}Si 2D MAF spectrum of Zhang et al. [78]. That is, knowledge of these five $Q^{(n)}$ isotropic chemical shift distributions allowed Florian and coworkers to fit

each J-resolved cross section to the appropriate number of J couplings, and use their relationship between the $^2J_{\text{Si-O-Si}}$ coupling and the Si–O–Si bond angle to determine the Si–O–Si bond angles associated with $Q^{(3)}$, $Q^{(2)}$, and $Q^{(1)}$ sites in a silicate glass for the first time.

Here we present the first of a multi-part solid-state NMR study to (1) determine the distribution of NMR parameters in a ^{29}Si enriched potassium disilicate glass ($K_2O \cdot 2\ SiO_2$), (2) establish relationships between NMR parameters and local structure, and (3) map measured NMR parameters distributions into structural distributions. The focus of this work is the accurate measurement of $Q^{(n)}$ populations in the potassium disilicate glass. Since its ^{29}Si MAS spectrum is completely unresolved, a simple deconvolution of the ^{29}Si MAS lineshape is not possible without additional assumptions to constrain the least-squares fit [52]. To avoid such assumptions we have utilized the 2D MAF technique to obtain accurate populations and the isotropic chemical shift distributions for each of the $Q^{(n)}$ sites. The MAF method also measures the full nuclear shielding anisotropy of each $Q^{(n)}$ site. Although less studied than the isotropic chemical shift, the nuclear shielding anisotropy can also serve a probe of the local structure [59,96–98]. Thus, another objective of this study is to obtain accurate nuclear shielding anisotropy data for further refinement of quantitative relationships to local structure.

2.2 Experimental

2.2.1 Nuclear Magnetic Resonance Spectroscopy

Experiments were performed on a hybrid Tecmag Apollo-Chemagnetics CMX II 9.4 Tesla (79.476 MHz for ^{29}Si) NMR spectrometer using a modified version of an

earlier DAS probe design [99]. The experiment was performed at ambient temperature with a sample spinning rate of 14 kHz. The ^{29}Si relaxation time was measured using the saturation recovery experiment under MAS condition and T_1 of 89 seconds was measured. A recycle delay of 6 minutes was chosen to prevent saturation. No changes in peak shape as a function of delay time were observed, indicating no differential relaxation among different species. For Bloch decay experiments a radio frequency (rf) strength of 42 kHz was used and 256 complex data points acquired.

The MAF pulse sequence used is shown in 2.1. This is a shifted-echo [100] version of the MAF experiment [79,80], where the MAS spectrum is correlated with spectrum while spinning at perpendicular to the external field. When spinning perpendicular the frequency anisotropies are scaled [76] by a factor of $-1/2$. In the MAF experiment the number of scans was 96 (following the application of 4 dummy scans), the number of $t_1 \times t_2$ points are 64×128, with dwell time of 62.5μs in t_1 and t_2. During the MAF experiment the magnetization is stored as Zeeman order during the hop of the rotor axis between angles. The value of τ_{hop} was 80 milliseconds. The echo shift time, τ_{echo}

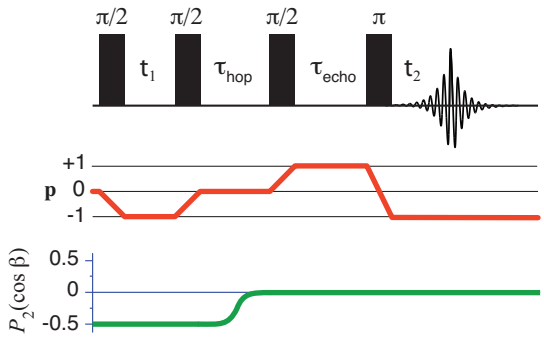

Figure 2.1: Shifted-echo Magic-Angle Flipping pulse sequence. Here t_1 is the evolution time at 90°, τ_{hop} is the time to flip the rotor between angles and τ_{echo} is the echo shift.

was 2.8 milliseconds. A Gaussian line shape convolution was applied to 2D MAF spectrum with standard deviations of 20 Hz and 100 Hz in the ω_1 and ω_2 dimensions, respectively.

In the discussion that follows we will employ the IUPAC definitions for the nuclear shielding and chemical shift interactions [64] outlined in Chapter One. The reference compound used was TMS

2.2.2 Sample Preparation

Approximately 450 mg of sample were synthesized from high purity K_2CO_3 (Aldrich, 99+%) and 96.74% ^{29}Si enriched SiO_2 (CortecNet). Before synthesis the SiO_2 was heat treated at 600°C for 5 hours in order to remove protons present in the sample, and was then kept and handled in an argon-filled glovebox. The starting materials were then decarbonated at 750°C for three hours, followed by melting for two hours at 1300°C. The sample was then quenched from this temperature down to room temperature by placing the bottom of the crucible into water. The weight loss during synthesis was within a few percent of nominal. The recovered sample was fully transparent and free of bubbles and was immediately put in an argon-filled glovebox for subsequent grinding. Rotor filling was performed in a argon-filled glove bag.

2.3 Results and Discussion

The one dimensional ^{29}Si MAS spectrum of $K_2O \cdot 2\ SiO_2$ glass is shown in 2.2. This spectrum has a broad resonance centered at -93 ppm, consistent with silicon predominately in a $Q^{(3)}$ coordination. Unlike our earlier study on the alkali silicate glass $2Na_2O \cdot 3\ SiO_2$, where overlapping but separate ^{29}Si resonances for $Q^{(2)}$ and $Q^{(3)}$ could be observed in the MAS spectrum, there is no clear resolution of $Q^{(n)}$-species

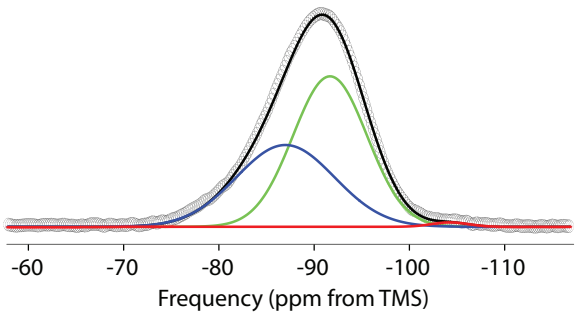

Figure 2.2: One dimensional ^{29}Si Magic-Angle Spinning Bloch Decay spectrum of $K_2O \cdot 2\ SiO_2$ glass along with "best-fit" model lineshape and component lineshapes for $Q^{(4)}$, $Q^{(3)}$, and $Q^{(2)}$ resonances. The spectrum baseline was corrected to eliminate any artifacts due to acquisition dead time.

in the MAS spectrum of the $K_2O \cdot 2\ SiO_2$ glass. As noted by Malfait *et al.* [52], the skew in the lineshape observed down field indicates $Q^{(2)}$ sites are present. Although ill posed, we performed a least-squares analysis of the MAS spectrum using three Gaussian lineshape components for a three site model of $Q^{(2)}$, $Q^{(3)}$, and $Q^{(4)}$. From this analysis we obtained 41.6%, 57.7%, and 0.7% for $Q^{(2)}$, $Q^{(3)}$, and $Q^{(4)}$ populations. Such a result, however, is clearly at odds with the prediction from the charge balance equation,

$$\mathrm{K/Si} = 4[Q^{(0)}] + 3[Q^{(1)}] + 2[Q^{(2)}] + [Q^{(3)}] \tag{2.1}$$

where our 1D MAS analysis yields a ratio of K/Si = 1.41 instead of K/Si = 1 expected for this composition.

2.3 shows the 2D contour plot of the ^{29}Si MAF spectrum for the $K_2O \cdot 2\ SiO_2$ glass. As illustrated elsewhere [77, 78] the five $Q^{(n)}$ sites have well defined differences in their ^{29}Si nuclear shielding tensors yielding characteristic anisotropic lineshapes that can distinguish between sites. In 2.3 one can see from the 90° dimension that

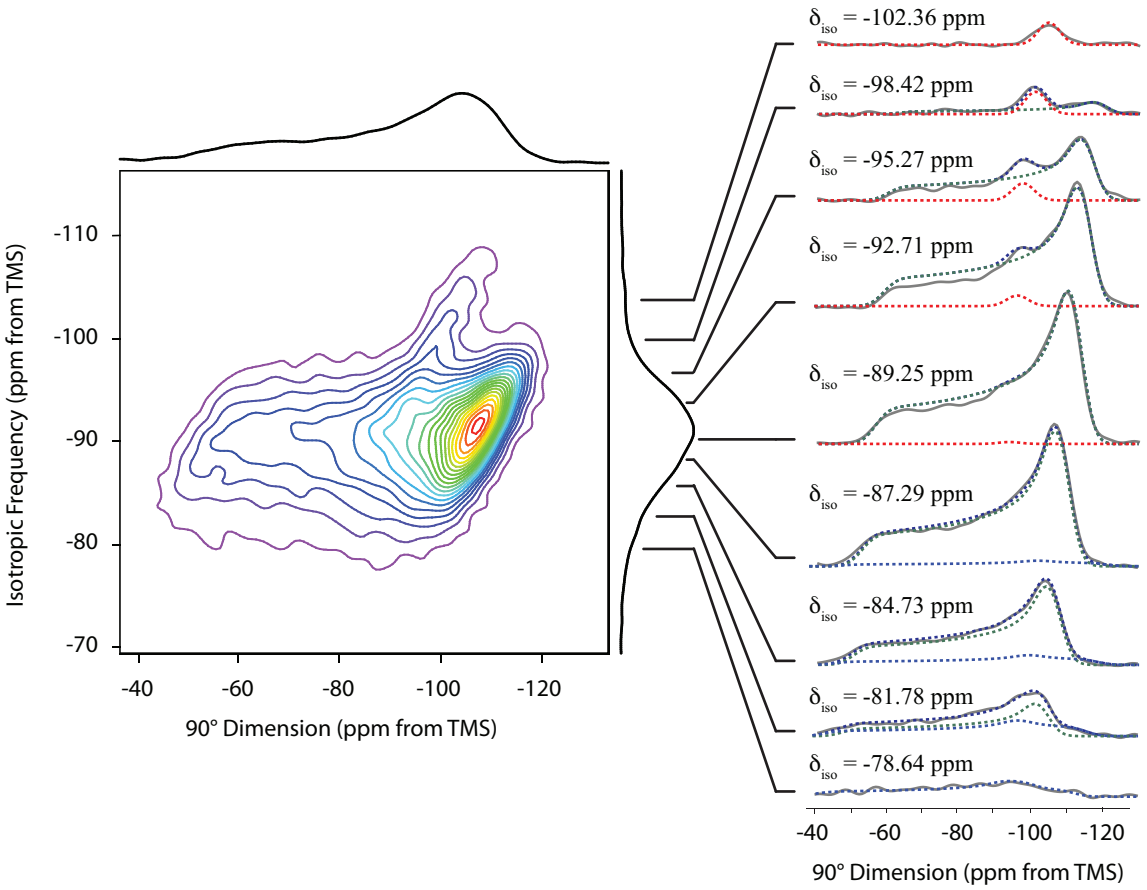

Figure 2.3: 2D ^{29}Si MAF NMR spectrum of $K_2O \cdot 2\ SiO_2$ glass (average reduced $\chi^2 = 2.51$). Twenty equally spaced contours are plotted from 5% to 95% of the maximum intensity. One-dimension projections onto the MAS and 90° dimensions. The 1D MAS projection is identical, within the noise level, to the 1D MAS spectrum of 2.2, indicating that there is no strong T_2 dependence on the MAS lineshape. Selected experimental cross sections (solid lines) are presented with spectral fits (dashed line).

Glass	ζ/ppm $Q^{(2)}$	$Q^{(3)}$	η $Q^{(2)}$	$Q^{(3)}$	ref.
$K_2O \cdot 2\ SiO_2$	-85.0 ± 1.3	-74.9 ± 0.2	0.48 ± 0.02	0.030 ± 0.006	this work
$2\ Na_2O \cdot 3\ SiO_2$	-78	-69	0.53	0.03	[77]
$CaO \cdot SiO_2$	-48.3	-45.4	0.70	0.01	[78]

Table 2.1: Nuclear shielding anisotropy parameters, ζ and η, for $Q^{(2)}$ and $Q^{(3)}$ measured in this work for $K_2O \cdot 2\ SiO_2$ compared to previous 2D MAF studies on $2\ Na_2O \cdot 3SiO_2$ [77], and on $CaO \cdot SiO_2$ [78].

the low intensities of the MAS lineshape around -105 ppm are dominated by $Q^{(4)}$, the MAS lineshape intensities around -90 ppm are dominated by $Q^{(3)}$, and the MAS lineshape intensities around -80 ppm have some contributions from $Q^{(2)}$.

The chemical shift anisotropy lineshapes in the individual cross-sections taken parallel to the 90° dimension were least-squares analyzed to obtain the relative contribution of each $Q^{(n)}$-species to the MAS intensity at the MAS frequency correlated to that cross-section. The anisotropic lineshape for each site was modeled using 5 parameters. These were (1) the isotropic chemical shift position δ_{iso}, (2) the chemical shift tensor anisotropy ζ, (3) the chemical shift tensor asymmetry parameter η, (4) the integrated intensity, and (5) a Gaussian line broadening. All sites in each cross-section shared the same isotropic chemical shift and that value was fixed by the isotropic dimension. In initial least-squares analyses those cross-sections dominated by one $Q^{(n)}$-species showed little variations in ζ, η, and Gaussian line broadening for the line shape of the dominant species. In cross-sections with strong overlap of $Q^{(n)}$-species and/or low signal-to-noise the least-squares analyses gave discontinuous

unphysical variations in the parameters. Therefore, in performing the final least-squares analysis of each cross-section the nuclear shielding tensor anisotropy ζ and asymmetry parameter η for a given $Q^{(n)}$ site were held fixed at the values obtained when that $Q^{(n)}$ site was the dominate species in the cross-section. Thus all sites were constrained to have the same optimized Gaussian line broadening of 563 Hz in the 90° dimension, with ζ and η fixed at $\zeta = -85.0 \pm 1.3$ ppm, $\eta = 0.48 \pm 0.02$ for $Q^{(2)}$, $\zeta = -74.9 \pm 0.2$ ppm, $\eta = 0.030 \pm 0.006$ for $Q^{(3)}$, and $\zeta = 0.0$ ppm, $\eta = 0.0$ for $Q^{(4)}$.

The magnitude of ζ values for both $Q^{(2)}$ and $Q^{(3)}$ are larger than those found in our previous 2D MAF studies on 2 $Na_2O \cdot 3SiO_2$ [77], and $CaO_2 \cdot SiO_2$ [78] glass as shown in 2.1. We find a strong correlation, shown in 2.4, between the ζ for $Q^{(2)}$ and $Q^{(3)}$ and the modifier cation field strength, calculated using the ionic radii of Whittaker and Muntus [101]. Even after taking into account the possibility of different modifier cation coordination numbers, indicted by roman numerals in 2.4, the correlation still appears to be relatively linear. This trend is consistent with previous observations by Stebbins [102]. It arises because the silicon–non-bridging oxygen distance increases with increasing modifier cation field strength, and as explained by Grimmer and coworkers [96, 97], a longer Si–O distance corresponds to less ^{29}Si shielding.

Shown in 2.3 are the 1D projections of the 2D spectrum onto the MAS and 90° dimensions. Additionally, selected 90° dimension cross sections associated with specific isotropic chemical shifts are shown with its "best fit" anisotropic lineshape along with component contributions. From the integrated area of each $Q^{(n)}$ component line shape in each 90° dimension cross section we construct the distribution of isotropic chemical shifts for each of the $Q^{(n)}$ resonances, shown in 2.5. Since the derived isotropic chemical shifts distributions appear to be approximately Gaussian each distribution was

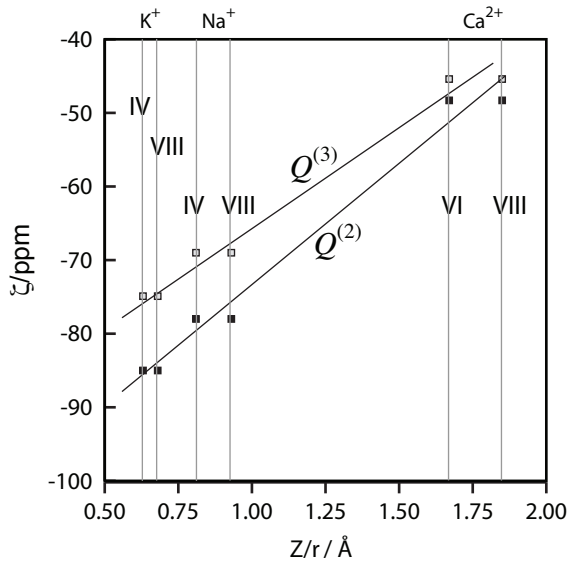

Figure 2.4: Nuclear shielding anisotropy, ζ, for $Q^{(2)}$ and $Q^{(3)}$ measured using ^{29}Si 2D MAF NMR as a function of of network modifier cation field strength, with roman numerals indicating different coordination number of modifiers X = K^+, Na^+, and Ca^{2+}.

fit to a Gaussian distribution to improve our accuracy in determining the integrated areas. The relative concentrations ($\pm$ one standard deviation) obtained from this analysis are given in 2.2 for the three $Q^{(n)}$-species. As mentioned earlier, it is important to emphasize that the distribution of the chemical shifts of each $Q^{(n)}$-species obtained from the 2D MAF analysis are not likely to match that obtained by a least-squares analysis of the 1D MAS spectrum, particularly when the MAS spectrum is unresolved, as was the case in 2.2.

Our measured MAF-derived populations agree with the expected K/Si ratio of the charge balance equation. Each $Q^{(n)}$-species has a charge of $-(4-n)$, which is balanced by the +1 charge of the potassium cations. For this composition the expected K/Si ratio is 1. The K/Si ratio calculated using Eq. (2.1) and the relative populations in 2.2

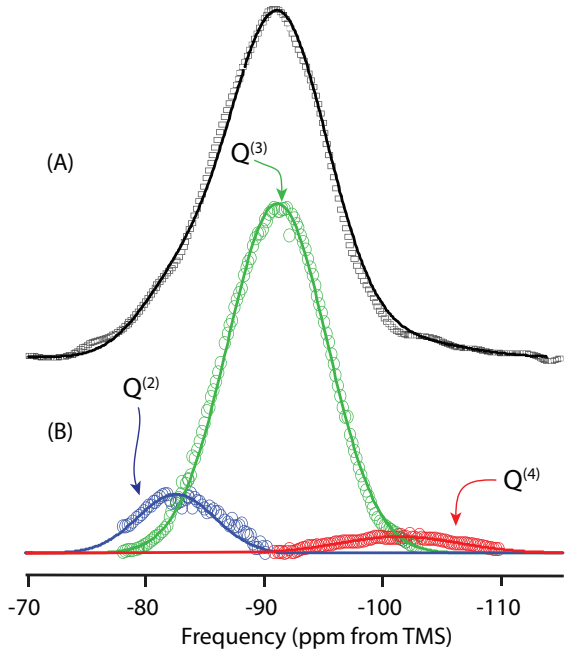

Figure 2.5: ^{29}Si NMR MAS results of (a) the isotropic projection of the 2D MAF dataset (squares) with the best fit (dashed line) and (b) and the integrated areas (circles) obtained from the simulated 2D MAF dataset with the Gaussian fits for each sites (solid lines).

is 1.026 ± 0.007. This value agrees reasonably well with the expected value and offers additional evidence that our measured populations are accurate. The slight deviation from unity is likely due to weight loss during synthesis and thus a slight change in stoichiometry. Some deviation could additionally arise from small defects in the glass network (uncompensated negative charge). The existence of small concentrations of $Q^{(2)}$ and $Q^{(3)}$ with different ζ and η, as observed by Maekawa et al. (1991) [60], could also affect measured concentrations, influencing the calculated potassium to silicon ratio, and interfere with the three site model used when fitting the 2D MAF dataset.

Site	Relative Area	Mean Position/ppm	Standard Deviation/ppm
$Q^{(2)}$	$9.8 \pm 0.7\%$	-82.74 ± 0.03	3.27 ± 0.03
$Q^{(3)}$	$83.0 \pm 0.1\%$	-91.321 ± 0.004	4.194 ± 0.003
$Q^{(4)}$	$7.2 \pm 0.3\%$	-101.67 ± 0.02	5.09 ± 0.03

Table 2.2: Gaussian distribution parameters of isotropic chemical shifts of $Q^{(n)}$-species in potassium disilicate glass derived from analysis of its 2D ^{29} MAF spectrum.

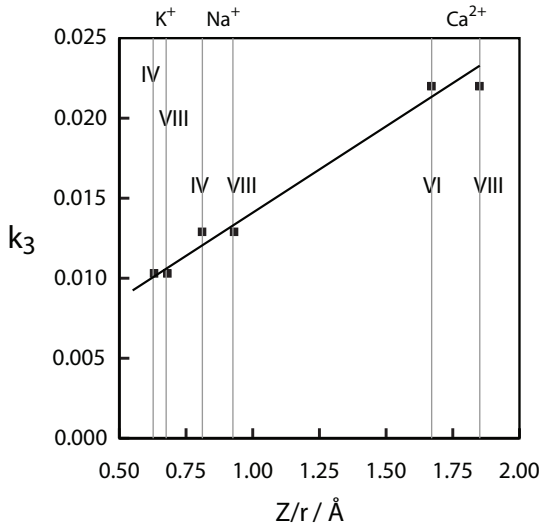

Figure 2.6: Disproportionation equilibrium constant, k_3, measured using ^{29}Si 2D MAF NMR as a function of of network modifier cation field strength.

A popular model, used in understanding the energetics and thermodynamic mixing properties of silicate melts [103, 104], and suggested as part of a mechanism for alkali ion transport in alkali silicate glasses [105, 106], involves the disproportionation equilibria between $Q^{(n)}$-species,

$$2Q^{(n)} \rightleftharpoons Q^{(n-1)} + Q^{(n+1)}, \tag{2.2}$$

with the equilibrium constant at the glass transition temperature,

$$k_n = [Q^{(n+1)}][Q^{(n-1)}]/[Q^{(n)}]^2. \tag{2.3}$$

The equilibrium constant for this disproportionation reaction ranges from $k_n = 0$ for a highly ordered (i.e. binary) distribution of silicate anionic species to $k_3 = 0.375$, $k_2 = 0.439$, and $k_1 = 0.311$ for a completely random distribution [107, 108]. Using the $Q^{(n)}$ populations obtained in this study we can calculate an equilibrium constant of $k_3 = 0.0103 \pm 0.0008$ for this composition. This value is consistent with previous studies [52,60,109] which indicate that potassium silicate glasses have a highly ordered distribution of silicate anionic species. Comparing this value with k_3 values obtained in our two previous 2D ^{29}Si MAF studies of 2 $Na_2O \cdot 3SiO_2$, and $CaO_2 \cdot SiO_2$ glass we observe a strong correlation between k_3 and modifier cation field strength, as shown in 2.6. The trend is consistent with earlier conclusions that higher charged cations shift the disproportionation reaction of Eq. (2.2) to the right [102, 110]. Even after taking into account the possibility of different modifier cation coordination numbers, indicted by roman numerals in 2.6, the correlation still appears to be relatively linear.

2.4 Summary

We have obtained and analyzed a 2D MAF spectrum of ^{29}Si enriched $K_2O \cdot 2\ SiO_2$ glass, whose 1D MAS spectrum is completely unresolved. By exploiting differences in ^{29}Si anisotropic lineshapes characteristic for each $Q^{(n)}$-species we have obtained accurate and quantitative $Q^{(n)}$ populations. Even though the spectral analysis was unconstrained by composition and charge balance, the $Q^{(n)}$ populations obtained were found to be consistent with those constraints. These $Q^{(n)}$ populations were used to calculate the equilibrium constant for the disproportion reaction of $Q^{(3)}$ occurring in the melt, and confirmed that a close to binary distribution of anionic species exists in the potassium disilicate glass. The observed k_3 value is also consistent with the expected trend of increasing $Q^{(n)}$ disproportionation with increasing network modifier cation strength. In fact, based on previous MAF studies of sodium and calcium silicate glasses it appears that this relationship may be close to linear. Finally, the nuclear shielding anisotropy observed for both $Q^{(2)}$ and $Q^{(3)}$ sites were found to be consistent with established trends in which the ^{29}Si nuclear shielding increases linearly with decreasing silicon–non-bridging oxygen bond length, which, in turn, increases when the non-bridging oxygen is coordinated by a modifier cation of lower field strength.

BIBLIOGRAPHY

[1] H. Tait, Five Thousand Years of Glass, British Museum Press, London, England, 1991.

[2] A. Oppenheim, R. H. Brill, D. Barage, A. von Saldern, Glass and Glassmaking in Ancient Mesopotamia. An edition of the cuneform texts which contain instructions for glassmakers, with a catlogue of surviving objects, The Corning Museum of Glass Press, Corning, New York, 1970.

[3] F. R. Matson, Glazed bricks in babylon-historical setting and microprobe analyses, Ceramics and Civilization (1985) 133–156.

[4] D. Grose, Innovation and change in ancient technologies: The anomalous case of the roman glass industry, Ceramics and Civilization 3 (1986) 65–79.

[5] E. Stern, Roman Mold Blown Glass, the First through Sixth Centuries, The Toledo Museum of Art, Toledo, Ohio, 1995.

[6] E. Stern, B. Schlick-Nolte, Fruhes Glas der alten Welt, Verlag Gerd Hatje, Stuttgart, Germany, 1995.

[7] R. Clay, T. Court, The History of the Microscope, Charles Grifin, London, England, 1932.

[8] B. Moody, The life of george ravenscroft, Glass Technology 29 (1988) 198–210.

[9] C. Zerwick, A Short History of Glass, The Corning Museum of Glass, Corning, New York, 1980.

[10] J. Dixon, J. Cann, C. Renfrew, Obsidian and the origins of trade, Scientific Anerican 29 (1968) 38–46.

[11] A. Markschies, The medival stained glass in the former cistercian monastery church of neuendorf, Historische Zeitschrift 292 (2011) 179–180.

[12] M. Cable, Classical glass technologies, Glass and Amorphous Materials 9.

[13] B. O. Mysen, P. Richet, Silicate Glasses and Melts, Properties and Structure, Elsevier, 2005.

[14] J. Zarzycki, Glasses and the Vitreous State, Cambridge Unversity Press, Cambridge, 1991.

[15] I. Fanderlik, Silica Glass and Its Applications, Elsevier, Amsterdam, Netherlands, 1990.

[16] G. Beall, Industrial Applications of Silica in Silica:Physical Behavior, Geochemistry and Materials Application, Mineralogical Society of AMerica, Washington D.C., USA, 1994.

[17] D. Foy, M. Vichy, M. Picon, Lingots de verre en mediterrancee occidentale, Annales du 14e congres de l'Association Internationale d'Histoire du Verre 3 (1998) 51–57.

[18] H. Dislich, Glastechn, Ber 44 (1971) 1.

[19] G. McCarthy, R. Roy, Gel route to homogenous glass preparation .2 gelling and desiccation, Journal of American Ceramics Society 54 (1971) 639.

[20] R. A. Weeks, D. Kinser, G. Kordas, 1st international conference on effects of modes of formation on the structure of glass, Journal of Non-Crystalline Solids 71 (1985) 1–456.

[21] R. A. Weeks, D. Kinser, 2nd international conference on effects of modes of formation on the structure of glass, Diffusion and Defect Data 53-4 (1985) 9–20.

[22] N. Platakis, H. Gatos, New flask evaporation method imporves film preparation, Journal of the Electrochemistry Society 123 (1976) 1409.

[23] P. Davidse, L. Maissel, Dielectric flims through rf sputtering, Journal of Applied Physics 37 (1966) 574.

[24] Y. Wada, M. Ashikawa, Oxidation characteristics of nitrogen implanted silicon, Japan Journal of Applied Physics 15 (1976) 1725.

[25] W. Kern, Chemical vapor-deposition systems for glass passivation of integrated circuits, Solid State Technologies 18 (1975) 25.

[26] W. Kern, G. Schnable, A. Fischer, Passivation coatings of silicon devices, RCA Review 37 (1976) 3.

[27] W. Kern, R. Rosler, Advances in deposition processes for passivation films, Journal of Vacuum Science Technologies 14 (1977) 1082.

[28] D. Secrist, J. Mackenzie, Solid state equilibria in systems lithium-carbon and lithium-boron, Bulletin of the American Ceramics Society 45 (1966) 784.

[29] G. Scherer, Sintering of low density glasses, Journal of the American Ceramics Society 60 (1977) 236.

[30] W. Primak, Electron bombardment investigation of dilatation in pile-exposed vitreous silica, Bulletin of of the American Physical Society 13 (1968) 74.

[31] R. Mozzi, B. Warren, Structure of vitreous silica, Journal of Appl. Cryst. 2 (1969) 164–172.

[32] T. Uchino, Y. Tokuda, T. Yoko, Vibrational dynamics of defect modes in vitreous silica., Physics Review B 58 (1998) 5322–5328.

[33] W. H. Zachariasen, The atomic structure in glass, J. Am. Chem. Soc. 54 (1932) 3841–3851.

[34] B. E. Warren, H. Krutter, O. Morningstar, Fourier analysis of x-ray patterns of vitreous SiO_2 and B_2O_3, J. Am. Ceram. Soc. 19 (1936) 202–206.

[35] B. E. Warren, J. Biscoe, Fourier analysis of X-ray patterns of soda-silica glass, J. Am. Ceram. Soc. 21 (1938) 259–265.

[36] A. C. Wright, Neutron scattering from vitreous silica. V. the structure of vitreous silica: What have we learned from 60 years of diffraction studies?, J. Non Cryst. Solids 179 (1994) 84–115.

[37] A. C. Wright, Neutron and x-ray amorphography, in: C. J. Simmons, O. H. El-Bayoumi (Eds.), Experimental Techniques of Glass Science, The American Ceramic Society, Westerville, OH, 1993, p. 205.

[38] J. Zarzycki, Congres intern. de verre, Trav. IV Szkice i materiay historyczne z XIX i XX wieku (1956) 323.

[39] J. Zarzycki, Sur l'angle de la liaison siosi de la silice vitreuse et celui de la liaison geoge de l'oxyde de germanium vitreux ou liquide, Verres et Refractaires 11 (1957) 3.

[40] E. Henniger, R. Buschert, Atomic structure and correlation in liquid binaries by x-ray and neutron diffraction with application to nak, Journal of Chemical Physics 44 (1966) 1758.

[41] R. L. Mozzi, B. E. Warren, The structure of vitreous silica, J. Appl. Cryst. 2 (1969) 164–172.

[42] J. Neuefeind, K.-D. Liss, Bond angle distribution in amorphous germania and silica, Berichte der Bunsen-Gesellschaft-Phys. Chem. Chem. Phys. 100 (8) (1996) 1341–1349.

[43] A. K. Varshneya, Fundamentals of Inorganic Glasses, Academic Press Inc., 1250 Sixth Avenue, San Diego, CA 92101, 1994.

[44] J. Zarzycki, Synthesis of glasses by hot-pressing of gels, Journal of Material Science 6 (1971) 130.

[45] G. N. Greaves, Exafs and the structure of glass, J. Non-Cryst. Solids 71 (1985) 203–217.

[46] P. J. Bray, NMR studies of the structures of glasses, J. Non Cryst. Solids 95 (1987) 45–60.

[47] W. G. Dorfeld, Structural thermodynamics of alkali silicates, Phys. Chem. Glasses 29 (1988) 179.

[48] R. Dupree, N. Ford, D. Holland, An examination of the ^{29}Si environment in the PbO-SiO_2 system by magic angle spinning nuclear magnetic resonance. part 1. glasses, Physics Chem. Glasses 28 (2) (1987) 78–84.

[49] J. F. Mammone, S. K. Sharma, M. F. Nicol, Ring structures in silica glass-a raman spectroscopic investigation, EOS 62 (1981) 425.

[50] F. L. Galeener, Planar rings in glasses, Solid State Communications 44 (1982) 1037.

[51] R. Barrio, F. Galeener, E. Martinez, R. Elliot, Regular ring dynamics in ax2 tetrahedral glasses, Physics Review B 48 (1993) 15672–15689.

[52] W. J. Malfait, W. E. Halter, Y. Morizet, B. H. Meier, R. Verel, Structural control on bulk melt properties: Single and double quantum ^{29}Si NMR spectroscopy on alkali-silicate glasses, Geochimica et Cosmochimica Acta 71 (2007) 6002–6018.

[53] S. K. Sharma, J. F. Mammone, M. F. Nicol, Raman investigation of ring configurations in vitreous silica, Nature 292 (1981) 140.

[54] P. F. McMillan, B. Piriou, A. Navrotsky, A raman spectroscopic study of glasses along the joins silica-calcium aluminate, silica-sodium aluminate, and silica-potassium aluminate, Geochim. Cosmochim. Acta 46 (1982) 2021–2037.

[55] F. L. Galeener, Band limits and the vibrational spectra of tetrahedral glasses, Physics Review B 19 (1979) 4292–4298.

[56] F. A. Seifert, B. Mysen, D. Virgo, Raman study of densified vitreous silica, Phys. Chem. Glasses 24 (1983) 141–145.

[57] N. Sen, M. Thorpe, Phonon in ax2 glasses: From molecular to band like modes, Phys. Rev. Letter B15 (1977) 4030–4038.

[58] E. Schneider, J. F. Stebbins, A. Pines, Speciation and local structure in alkali and alkaline earth silicate glasses: Constraints from ^{29}Si NMR spectroscopy, J. Non Cryst. Solids 89 (1987) 371–383.

[59] J. F. Stebbins, Identification of multiple structural species in silicate glasses by ^{29}Si NMR, Nature 330 (1987) 465.

[60] H. Maekawa, T. Maekawa, K. Kawamura, T. Yokokawa, The structural groups of alkali silicate glasses determined from ^{29}Si MAS-NMR, J. Non-Cryst. Solids 127 (1991) 53–64.

[61] A. E. Geissberger, P. J. Bray, Determinations of structure and bonding in amorphous SiO_2 using ^{17}O NMR, J. Non-Cryst. Solids 54 (1983) 121.

[62] R. Dupree, D. Holland, P. W. McMillan, R. F. Pettifer, The structure of soda-silica glasses: A MAS NMR study, J. Non-Cryst. Solids 68 (1984) 399.

[63] K. A. Smith, R. J. Kirkpatrick, E. Oldfield, D. M. Henderson, High-resolution silicon-29 nuclear magnetic resonance spectroscopic study of rock-forming silicates, Am. Mineral. 68 (1983) 1206–1215.

[64] R. K. Harris, E. D. Becker, S. M. C. D. Menezes, P. Grangerd, R. E. Hoffman, K. W. Zilm, Further conventions for NMR shielding and chemical shifts, IUPAC recommendations 2008, Inorg. Chem. 3 (2008) 41–56.

[65] I. J. Lowe, Free induction decays of rotating solids, Phys. Rev. Lett. 2 (1959) 285–287.

[66] A. Samoson, E. Lippmaa, Sychronized double-rotation NMR spectroscopy, J. Magn. Reson. 84 (1989) 410.

[67] A. Samoson, E. Lippmaa, 2D NMR nutation spectroscopy in solids, J. Magn. Reson. 79 (2) (1988) 255–268.

[68] A. Samoson, E. Lippmaa, A. Pines, High resolution solid-state NMR. Averaging of second-order effects by means of a double-rotor, Mol. Phys. 65 (1988) 1013.

[69] H. Eckert, Structural characterization of noncrystalline solids and glasses using solid state NMR, Prog. NMR Spectroscopy 24 (1992) 159.

[70] C. M. Schramm, B. H. W. S. d. Jong, V. E. Parziale, ^{29}Si magic angle spinning NMR study on local silicon environments in amorphous and crystalline lithium silicates, J. Am. Chem. Soc. 106 (1984) 4396.

[71] W. Malfait, W. Halter, R. Verel, Si-29 NMR spectroscopy of silica glass: T-1 relaxation and constraints on the Si-O-Si bond angle distribution, Chem. Geol. 256 (2008) 269–277.

[72] H. Maekawa, T. Nakao, S. Shimokawa, T. Yokokawa, Coordination of sodium ions in $NaAlO_2$-SiO_2 melts: A high temperature Na-23 NMR study, Phys. Chem. Min. 24 (1997) 53.

[73] A. Bax, N. M. Szeverenyi, G. E. Maciel, Correlation of isotropic shifts and chemical shift anisotropies by two-dimensional Fourier-transform magic-angle hopping NMR spectroscopy, J. Magn. Reson. 52 (1983) 147.

[74] W. T. Dixon, Spinning-sideband-free and spinning-sideband-only NMR spectra in spinning samples, J. Chem. Phys. 77 (1982) 1800.

[75] O. N. Antzutkin, S. C. Shekar, M. H. Levitt, Two-dimensional sideband separation in magic-angle spinning NMR, J. Magn. Reson. A 115 (1995) 7–19.

[76] M. Mehring, High Resolution NMR Spectroscopy in Solids, Vol. 11, Springer-Verlag, Berlin, 1983.

[77] P. Zhang, C. Dunlap, P. Florian, P. J. Grandinetti, I. Farnan, J. F. Stebbins, Silicon site distributions in an alkali silicate glass derived by two-dimensional ^{29}Si nuclear magnetic resonance, J. Non. Cryst. Solids 204 (1996) 294–300.

[78] P. Zhang, P. J. Grandinetti, J. F. Stebbins, Anionic species determination in $CaSiO_3$ glass using two-dimensional ^{29}Si NMR, J. Phys. Chem. B 101 (20) (1997) 4004–4008.

[79] A. Bax, N. M. Szeverenyi, G. E. Maciel, Chemical shift anisotropy in powdered solids studied by 2D FT NMR with flipping of the spinning axis, J. Magn. Reson. 55 (1983) 494.

[80] P. J. Grandinetti, Y. K. Lee, J. H. Baltisberger, B. Q. Sun, A. Pines, Sideband patterns in dynamic-angle spinning NMR, J. Magn. Reson. A 102 (1993) 195.

[81] Z. H. Gan, High-resolution chemical-shift and chemical-shift anisotropy correlation in solids using slow magic-angle spinning, J. Am. Chem. Soc. 114 (21) (1992) 8307–8309.

[82] J. Z. Hu, D. W. Alderman, C. H. Ye, R. J. Pugmire, D. M. Grant, An isotropic chemical shift-chemical shift anisotropy magic-angle slow-spinning 2D NMR experiment, J. Magn. Reson. A 105 (1) (1993) 82–87.

[83] J. C. C. Chan, R. Tycko, Recoupling of chemical shift anisotropies in solid-state NMR under high- speed magic-angle spinning and in uniformly ^{13}C-labeled systems, J. Chem. Phys. 118 (2003) 8378–8389.

[84] M. J. Duer, S. R. Elliot, L. F. Gladden, An investigation of the structural units in sodium disilicate glass: a 2-d ^{29}Si NMR study, J. Non Cryst. Solids 189 (1995) 107–117.

[85] F. Fayon, C. Bessada, A. Douy, D. Massiot, Chemical bonding of lead in glasses through isotropic vs anisotropic correlation: Pass shifted echo, J. Magn. Reson. 137 (1999) 116–121.

[86] L. Montagne, S. Donzea, G. Palavita, J. C. Boivina, F. Fayon, D. Massiot, J. Grimblot, L. Gengembrec, ^{207}Pb and ^{113}Cd NMR and XPS characterization of PbO-$PbCl_2$-$CdCl_2$ glasses, J. Non-Cryst. Solids 293-295 (2001) 74–80.

[87] F. F. Slejko, R. Petrini, C. Forte, G. Pedrazzi, C. Pinzino, M. D'Antonio, The structure of dense and vesiculated volcanic glass fragments from the astroni tephra (phlegraean fields, italy) explored by spectroscopic techniques: implications on bubble expansion and dynamics of magma ascent, J. Non. Cryst. Solids 323 (2003) 54–67.

[88] D. Sakellariou, J.-F. Jacquinot, T. Charpentier, 2D correlation spectra of isotropic and anisotropic ^{29}Si chemical shifts in crystalline and amorphous natural abundance materials under very slow sample rotation, Chem. Phys. Lett. 411 (2005) 171–174.

[89] D. Sakellariou, T. Charpentier, Shift anisotropy tensors in amorphous natural-abundance solids: High-resolution ^{29}Si chemical shift anisotropy distributions under very slow sample rotation, Appl. Magn. Reson. 32 (2007) 583–594.

[90] M. Feike, C. Jäger, H. W. Spiess, Connectivities of coordination polyhedra in phosphates glasses from ^{31}P double-quantum NMR spectroscopy, J. Non-Cryst. Solids 223 (1998) 200–206.

[91] R. Witter, P. Hartmann, J. Vogel, C. Jäger, Measurements of chain length distribution in chain phosphate glasses using 2D ^{31}P double quantum NMR, Solid State NMR 13 (1998) 189–200.

[92] K. Glock, O. Hirsch, P. Rehak, B. Thomas, C. Jäger, Novel opportunities for studying this short and medium range order of glasses by MAS NMR, ^{29}Si

NMR and IR spectroscopies, Journal of Non-Crystalline Solids 232-234 (1998) 113–118.

[93] L. Olivier, X. Yuan, A. N. Cormack, C. Jäger, Combined ^{29}Si double quantum NMR and MD simulation studies of network connectivities of binary $Na_2O \cdot SiO_2$ glasses: new prospects and problems, J. Non-Cryst. Solids 293-295 (2001) 53–66.

[94] F. Fayon, G. L. Saout, L. Emsley, D. Massiot, Through-bond phosphorus-phosphorus connectivities in crystalline and disordered phosphates by solid-state NMR, Chem. Comm. (2002) 1702–1703.

[95] P. Florian, F. Fayon, D. Massiot, ^2J Si–O–Si scalar spin-spin coupling in the solid state: Crystalline and glassy wollastonite $CaSiO_3$, J. Phys. Chem. C 113 (2009) 2562–2572.

[96] A.-R. Grimmer, E. F. Gechner, G. Molgedey, High resolution ^{29}Si NMR in solid silicates. correlations between shielding tensor and Si-O bond length, Chem. Phys. Lett. 77 (1981) 331–335.

[97] A.-R. Grimmer, Correlation between individual Si-O bond lengths and the principal values of the ^{29}Si chemical-shift tensor in solid silicates, Chem. Phys. Lett. 119 (1985) 416–420.

[98] M. R. Hansen, H. J. Jakobsen, J. Skibsted, ^{29}Si chemical shift anisotropies in calcium silicates from high-field ^{29}Si MAS NMR spectroscopy, Inorg. Chem. 42 (7) (2003) 2368–2377.

[99] M. A. Eastman, P. J. Grandinetti, Y. K. Lee, A. Pines, Double-tuned hopping-coil probe for dynamic-angle spinning NMR, J. Magn. Reson. 98 (1992) 333–341.

[100] P. J. Grandinetti, J. H. Baltisberger, A. Llor, Y. K. Lee, U. Werner, M. A. Eastman, A. Pines, Pure absorption-mode lineshapes and sensitivity in two-dimensional dynamic angle spinning NMR, J. Magn. Reson. A 103 (1993) 72–81.

[101] E. J. W. Whittaker, R. Muntus, Ionic radii for use in geochemistry, Geochim. Cosmochim. Acta 34 (1970) 945–956.

[102] J. F. Stebbins, Effects of temperature and composition on silicate glass structure and dynamics: Si-29 NMR results, J. Non Cryst. Solids 106 (1988) 359–369.

[103] A. Navrotsky, Energetics of silicate melts, in: J. F. Stebbins, P. F. McMillan, D. B. Dingwell (Eds.), Structure , Dynamics and Properties of Silicate Melts, Vol. 32 of Reviews in Mineralogy, Mineralogical Society of America, Washington, DC, 1995, pp. 121–143.

[104] P. C. Hess, Thermodynamic mixing properties and the structure of silicate melts, in: J. F. Stebbins, P. F. McMillan, D. B. Dingwell (Eds.), Structure , Dynamics and Properties of Silicate Melts, Vol. 32 of Reviews in Mineralogy, Mineralogical Society of America, Washington, DC, 1995, pp. 145–190.

[105] G. N. Greaves, S. J. Gurman, C. R. A. Catlow, A. V. Chadwick, S. Houde-Walter, C. M. B. Henderson, B. R. Dobson, A structural basis for ionic diffusion in oxide glasses, Phil. Mag. A 64 (1991) 1059–1072.

[106] M. D. Ingram, Ionic conductivity and glass structure, Phil. Mag. B 60 (1989) 729.

[107] B. Vessal, A. C. Wright, A. C. Hannon, Alkali silicate glasses: Interpreting neutron diffraction results using the molecular dynamics simulation technique, J. Non Cryst. Solids 196 (1996) 233–238.

[108] E. D. Lacy, A statistical model of polymerisation/depolymerisation relationship in silicate melts and glasses, Phys. Chem. Glasses 6 (5) (1965) 171–180.

[109] V. P. Zakaznova-Herzog, W. J. Malfait, F. Herzog, W. E. Halter, Quantitative Raman spectroscopy: Principles and application to potassium silicate glasses, Journal of Non-Crystalline Solids 353 (2007) 4015–4028.

[110] J. B. Murdoch, J. F. Stebbins, I. S. E. Carmichael, High-resolution ^{29}Si NMR study of silicate and aluminosilicate glasses: the effect of network-modifying cations, Am. Mineral. 70 (1985) 332–343.